

## APPLIED RESEARCH

# AI-Based Hydraulic and Electrical Fault Identification in Direct-Driven Hydraulic Systems

VIACHESLAV ZAKHAROV<sup>1</sup>, VAN KHANG HUYNH<sup>2</sup>,  
AND TATIANA MINAV<sup>1</sup>, (Member, IEEE)

<sup>1</sup>Faculty of Engineering and Natural Sciences (ENS), Tampere University, 33720 Tampere, Finland

<sup>2</sup>Department of Engineering Science, University of Agder, 4879 Grimstad, Norway

Corresponding author: Viacheslav Zakharov (viacheslav.zakharov@tuni.fi)

This work was supported in part by the Business Finland Project EMMA-2 under Grant 2471/31/2021.

**ABSTRACT** Direct drive hydraulic (DDH) systems present a promising alternative to traditional systems in off-road mobile machinery (NRMM) due to their energy efficiency, improved controllability, and lower maintenance costs. Such systems combine both electrical and hydraulic components that are subject to wear and tear and require fault identification, both individually and in combination. Since all system elements are interconnected hydraulically, mechanically, or electrically, changes in the behavior of some components directly affect the operation of others. Consequently, this paper explores an AI-based fault diagnosis method that uses only electrical signals from an electric motor, while simultaneously identifying both hydraulic and electrical faults in DDH systems, eliminating the need for supplementary sensors. This method was tested in an experiment that combines a physical emulation of the hydraulic part of the system based on mathematical modeling and work with an electric motor with real faults. The study covers various faults such as inter-turn winding short circuits, internal cylinder leakage, and gear pump and check valve faults. The obtained data underwent multi-stage preprocessing, as well as machine learning algorithms, mainly support vector machine (SVM) with different kernels, resulting in an overall classification accuracy above 84% in three-fourths of the tested scenarios, with about half exceeding 90%. A masking effect was also observed, where an inter-turn short circuit fault partially obscures the signatures of some hydraulic faults. The obtained results prove the effectiveness and prospects of the proposed fault diagnosis method in both DDH and other electro-hydraulic systems. Such a method can increase the probability of timely fault detection, thereby reducing downtime and maintenance costs while significantly increasing the efficiency of NRMM.

**INDEX TERMS** Artificial intelligence, condition monitoring, cylinder leakage, direct-driven hydraulics (DDH), electric signal analysis, electro-hydraulic systems, fault diagnostics, hydraulic system monitoring, machine learning, non-road mobile machinery (NRMM), predictive maintenance, pump defect, rotor demagnetization, support vector machine (SVM), winding short circuit.

## I. INTRODUCTION

Non-road mobile machinery (NRMM) includes various types of machines used in construction, mining, agriculture, warehousing, and other industries [1]. These industries require high power, a wide range of performance characteristics, and machine reliability. At the same time, NRMM,

as with other types of industrial equipment, is subject to strict environmental requirements. In recent decades, many countries have chosen a path of development that aims to reduce polluting emissions, leading to the need for new and more efficient solutions [2]. For example, the European Union has been continuously updating a series of directives first developed in the late 1990s (from Directive 97/68/EC to the modern Stage V standards) for a long time, with the aim of reducing CO<sub>2</sub> and particulate emissions [3]. One

The associate editor coordinating the review of this manuscript and approving it for publication was Qinfen Lu<sup>1</sup>.

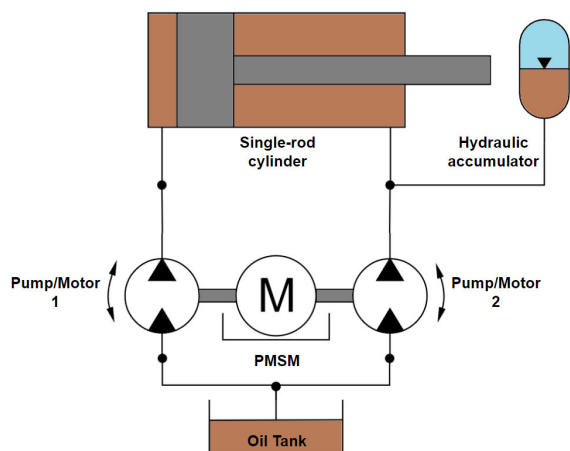


FIGURE 1. DDH system.

of the leaders in such initiatives is Finland, which has set an ambitious goal of achieving carbon neutrality by 2035. Such practices place additional pressure on the NRMM industry [4].

One of the most promising areas in the development of NRMM is the hybridization and electrification of systems, both partial and complete. Electric motors (EMs) offer numerous advantages over traditional internal combustion engines (ICE), such as significantly higher efficiency, reduced acoustic emissions, improved controllability, wider control range, low operating costs, simplicity, and reliability [5]. Despite the fact that hybrid machines have their advantages, they are considered to be a transitional step to fully electric machines, which are perceived as the most promising direction, especially in terms of polluting emissions [6], [7]. In the field of hydraulic systems, this situation has led to the emergence of direct-driven hydraulics (DDH) architecture. DDH is a system, where the EM is directly (mechanically) connected to the pumps, providing high dynamic characteristics and efficiency [8]. In addition, less apparent advantages include reduced maintenance costs and a more compact design [9], [10], [11]. A schematic of the DDH system is represented in Figure 1

Compared to traditional hydraulic systems, DDH systems feature a complete interconnection between the electrical, mechanical, and hydraulic parts of the system, which are mutually interdependent [12], [13]. This component interconnection, which incorporates advanced EM technologies and artificial intelligence, opens up a wide range of possibilities, such as the implementation of condition monitoring systems [14]. However, due to this same interconnection, DDH systems can have negative effects, complicating their detection, since disturbances in one part can propagate as hydraulic, mechanical, or electrical vibrations [14], [15].

Previous studies have considered various methods of condition monitoring in DDH systems. For example, a study involving modeling and simulation of systems with faulty check valves yielded encouraging results, demonstrating an accuracy of at least 70% in detecting hydraulic system faults

by analyzing both hydraulic and electrical information [16]. In that work, five different check-valve faults were simulated and analyzed directly in the time domain using measurements from both the hydraulic and electrical subsystems. However, in scenarios where only one type of data is used (e.g., electrical), fault detection becomes difficult due to the distortion of information when transforming energy from one form to another, especially under data constraints.

To address this issue, one previous study [17] applied advanced statistical methods to process the electrical data and explicitly evaluated how both the modulation method and the electric-drive structure influence the fault-detection accuracy. Using only electrical signals obtained from the motor, without any hydraulic sensors, that approach achieved accuracy levels ranging from 75% to 96% depending on the scenario.

Despite these achievements, many problems remain unsolved. In particular, recent studies have either insufficiently addressed, or failed to address, the influence of cross-talk between the hydraulic and electrical parts of the system, especially when faults occur [18]. This raises two critical questions: (1) “With what accuracy can faults in DDH systems be detected using AI-based condition-monitoring methods?” and (2) “What is the influence of different types of faults on one another, in terms of detection accuracy?”

To answer these questions, the present study investigates an AI-based diagnostic approach that uses only the electrical signals from the electric motor to identify both hydraulic and electrical faults within a DDH system. The approach is experimentally validated using hybrid fault scenarios that combine modeled hydraulic and real electrical faults, providing insight into how cross-talk between system components affects diagnostic performance and achievable fault-detection accuracy under different operating conditions.

For this purpose, a DDH setup capable of exhibiting both hydraulic and electrical faults was employed. A dynamic model of the hydraulic subsystem was developed in Matlab/Simulink and integrated with an experimental test rig consisting of two permanent magnet synchronous motors (PMSMs). The electrical signals from one PMSM were used as the input data for diagnosing individual and combined faults. The collected data underwent multi-stage statistical and machine-learning-based processing to classify the different fault scenarios and evaluate the effectiveness of the proposed method.

The remainder of the article is organized as follows. Section II, describes the mathematical modeling of the system, including hydraulic and electrical components, as well as the fault realization. Section III describes the experimental setup, the utilized components, and the selection of the testing mode. Section IV explains the experimental methodology, covering fault scenarios and data collection. Section V discusses the data processing methods, including the pre-processing steps, feature selection, and classification algorithms. Section VI analyzes the obtained results, evaluating the classification accuracy and the influence of various

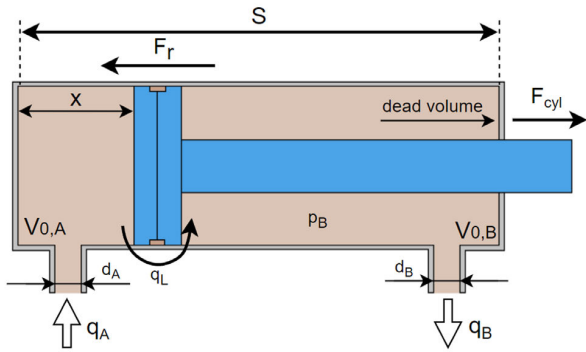


FIGURE 2. Single-rod cylinder, its dimensions, and forces.

factors on the diagnosis. Finally, the primary conclusions are drawn in Section VII.

## II. MODELING

In this study, a DDH system is integrated into an experimental setup for controlling the lifting mechanism of a mobile crane. Two operating modes of the setup are considered lifting (i.e., extending the cylinder rod) and lowering (i.e., retracting the cylinder rod) of the boom under load. A PMSM under field-oriented control is used as a prime mover. This model is capable of providing high accuracy across the entire dynamic range, which was demonstrated in previous studies [16], [17]. In addition, it also supports the simulation of five different check-valve faults, of which two (leakage and deadband faults) are investigated in this research.

Section A details the modeling of an internal leakage in a hydraulic cylinder, simulating pressure loss due to seal degradation. Section B describes the modeling of a fault in the gear pump caused by a damaged gear tooth, leading to pulsations in flow and torque. These fault scenarios are integrated into a comprehensive simulation framework, forming the basis for experimental validation and fault classification.

### A. CYLINDER INTERNAL LEAKAGE

Internal cylinder leakage can occur due to wear of the piston seals in the hydraulic cylinder, leading to uncontrolled movement of fluid between the piston and rod chambers. As a result, the effective pressure in the cylinder will decrease, and the output force with control accuracy will decrease [19]. In practice, this can lead to a slowing down or loss of stability of the rod movement, which is critical for systems under load [20].

The original model describes the fluid flows in the cylinder chambers based on the external inlet and outlet flows. In the presence of an internal leak, an additional flow  $q_{leak}$  arises depending on the pressure difference between Chambers A and B:

$$q_{leak} = C_l(p_a - p_b), \quad (1)$$

where  $p_a$  and  $p_b$  are the pressures in Chambers A and B respectively and  $C_l$  is the leakage coefficient, which depends

on the clearance between the piston and the cylinder, as well as the fluid viscosity.

$$C_l = \frac{\pi h^3}{12\mu L}, \quad (2)$$

where  $h$  is the radial clearance between the piston and the cylinder,  $L$  is the leakage path length (approximately equal to the width of the seal), and  $\mu$  is the dynamic viscosity of the fluid. The presence of the specified leakage flow directly affects all forces and processes associated with the cylinder. An image of the cylinder demonstrating flows and forces is illustrated in Figure 2.

The volumes of the cylinder chambers are written further.

$$V_a = V_{0,a} + A_a x, \quad (3)$$

$$V_b = V_{0,ab} + A_b(s - x), \quad (4)$$

where  $V_a$  is the volume of Chamber A,  $V_b$  is the volume of Chamber B,  $V_{0,a}$  and  $V_{0,b}$  are the volume of Chambers A and B, respectively,  $s$  is the piston stroke length, and  $x$  is the position of the piston,  $A_a$  is the effective area of the piston in the A chamber,  $A_b$  is the effective area of the piston in the B chamber.

To describe the pressure in the chambers, a model employs the equation for pressure variation in a closed volume. In this model, external leaks are not taken into account, and the pressure is distributed uniformly throughout the chamber. As a result, the changes in pressure in Chambers A and B were obtained as follows:

$$\frac{dp_a}{dt} = \frac{B(p)}{V_a} \left( q_a - A_a \frac{dx}{dt} - q_{leak} \right), \quad (5)$$

$$\frac{dp_b}{dt} = \frac{B(p)}{V_b} \left( q_b - A_b \frac{dx}{dt} + q_{leak} \right), \quad (6)$$

where  $p_a$  and  $p_b$  are the pressures in the respective chambers,  $B(p)$  is the bulk modulus, and  $q_a$  and  $q_b$  are the flow rates in and out of the cylinder, respectively. The resulting pressures can be then translated into acting forces acting on the cylinder piston. Taking into account additional forces such as friction force  $F_{fr}$  and end force  $F_{end}$  (i.e., the force arising when the piston rests against the cylinder walls) of the cylinder, we can derive an equation for the resulting force created by the cylinder.

$$F_{cyl} = F_a - F_b - F_{fr} - F_{end}, \quad (7)$$

The flow of fluid passing through a cylinder orifice is described by the Ellman-Piché equation. This equation allows the flow to be calculated in discrete solvers.

$$q_{or} = \begin{cases} C_q A_0 \sqrt{\frac{2\Delta p_{or}}{\rho}}, & \Delta p_{or} > p_{tr} \\ \frac{3A_0 \nu R_{tr}}{4D} \cdot \frac{\Delta p_{or}}{p_{tr}} \left( 3 - \frac{\Delta p_{or}}{p_{tr}} \right), & 0 \leq \Delta p_{or} \leq p_{tr}, \end{cases} \quad (8)$$

$$p_{tr} = \frac{9R_{tr}\rho\nu^2}{8C_q^2 D^2}, \quad (9)$$

where  $C_q$  is the discharge coefficient,  $R_{tr}$  is the transition Reynolds number,  $D$  is the orifice diameter,  $\nu$  is the kinematic viscosity of the fluid, and  $q_{or}$  is the flow through the orifice, and  $\Delta p_{or}$  is the pressure drop across the orifice. Taking into account the flow caused by the leakage,  $\Delta p_{or}$  can be calculated as follows:

$$\Delta p_{or} = |p_a - p_b| - C_l(p_a - p_b)R_{leak}, \quad (10)$$

where  $R_{leak}$  is the hydraulic resistance of the leakage.

### B. DAMAGED GEAR TOOTH IN AN AXIAL-PISTON PUMP

In gear pumps, power is transmitted through a gear mechanism. Its damage (usually in a gear tooth) causes uneven fluid flow, which leads to pressure pulsations, vibrations, and noises. Such phenomena affect the entire system and can even cause resonant oscillations, accelerating the wear of other system components. The hydraulic pump model was implemented using the Schlösser flow loss and torque model. Since damage to a gear tooth in the pump causes uneven flow and local pressure pulsations, the original model undergoes certain changes [21]. This failure causes an increase in the laminar and turbulent leakage coefficients  $C_S$  and  $C_{St}$  due to increased clearances and unstable flow [22].

$$q_L = (C_S + \Delta C_S) \frac{V_p \Delta p_p}{2\pi \rho \mu} + (C_{St} + \Delta C_{St}) V_p^{\frac{2}{3}} \sqrt{\frac{2|\Delta p_p|}{\rho}} + q_{puls}, \quad (11)$$

where,  $q_L$  is the flow loss,  $V_p$  is the the pump displacement per revolution,  $\Delta p_p$  is the pressure drop in the pump,  $\rho$  is the density of the working fluid,  $\mu$  is the dynamic viscosity of the fluid,  $q_{puls}$  is the pulsating flow. As can be seen, additional losses  $\Delta C_S$  and  $\Delta C_{St}$  were added to the final equation of the flow created by the pump. The calculation of these values was performed as an empirical method, taking into account the degree of wear on the gear tooth:

$$\Delta C_S = k_S C_S, \quad \Delta C_{St} = k_{St} C_{St}, \quad (12)$$

$$\Delta C_{St} = k_{St} C_{St}, \quad (13)$$

$$k_S = k_{St} = \frac{\Delta g}{g}, \quad (14)$$

where,  $g$  is the nominal clearance between pump components and  $\Delta g$  is the the increase in clearance due to wear.

Additional flow pulsations  $q_{puls}$  caused by the fault were implemented using a periodic function. Taking into account the dynamic mode of the system, an exponentially decaying pulse function was chosen. This function allows for simulating ‘‘abrupt’’ changes in flow when passing a broken tooth, while ensuring smooth attenuation of surges when the gear rotates.

$$q_{puls}(t) = A_q \sum_{n=-\infty}^{\infty} e^{-\beta(t-nT)} H(t - nT), \quad (15)$$

where,  $A_q$  is the flow impulse amplitude,  $\beta$  is the damping coefficient,  $T$  is the the period of pulsations,  $H$  is the

Heaviside function, and  $n$  is the the revolution number. The impulse period can be calculated as follows:

$$T = \frac{60}{N_p n_p}, \quad (16)$$

where,  $N_p$  is the number of teeth and  $n_p$  is the rotation speed.

The torque equation created by the pump also undergoes changes, since such a failure creates additional resistance during power transmission, increasing friction losses and impact loads. In the torque model, the friction coefficients  $C_f$  and  $C_h$  increase, reflecting the increased load on the transmission elements.

$$T_L = (C_f + \Delta C_f) \frac{V_p \Delta p_p}{2\pi} + \mu V_p n_p + (C_h + \Delta C_h) \frac{V_p^{\frac{5}{3}} n_p^2}{4\pi} + T_{sh}, \quad (17)$$

$$\Delta C_f = \frac{\Delta \mu}{2\pi r} + \frac{\mu \Delta r}{2\pi r^2}, \quad (18)$$

$$\Delta C_h = \frac{\Delta \eta}{\rho r^2} + \frac{2\eta \Delta r}{\rho r^3}, \quad (19)$$

where,  $\Delta \mu$  is the friction coefficient difference, and  $\Delta r$  is the contact radius difference,  $\eta$  is the effective viscosity difference. Since the oil temperature is taken as constant, the coefficient of viscous friction  $\mu$  remains constant.

An approximate evaluation of  $\Delta C_f$  and  $\Delta C_h$  thus follows:

$$\Delta C_f \approx k C_f, \quad k \in [0, 1], \quad (20)$$

$$\Delta C_h \approx k C_h, \quad k \in [0, 1], \quad (21)$$

where,  $k$  is the degree of gear tooth wear.

To implement additional shock loads in the form of sharp changes in torque caused by a gear tooth breakage, a periodic function was also used.

$$T_{Sh} = A_{Sh} \sum_{n=-\infty}^{\infty} e^{-\beta(t-nT)} H(t - nT), \quad (22)$$

where,  $A_{Sh}$  is an impulse torque amplitude.

Since the validation of the ‘‘good model’’ has already been carried out in previous studies, and the fault realization is based on sound arguments and preliminary calculations, it can be concluded that the developed hydraulic system model successfully reproduces hydraulic responses under given pump speeds and load conditions.

### III. TEST RIG DESCRIPTION

This section describes the experimental setup assembled to investigate fault detection in an electro-hydraulic system where a PMSM is used as a prime mover. The objective of this setup is to simulate the behavior of the overhead crane utilized in the earlier studies. Leveraging the resources of the University of Agder, it was possible to use not only healthy EMs but also faulty ones in the experiment, which significantly enhances the validity of the study. A detailed description of the setup and the fault types is presented below.

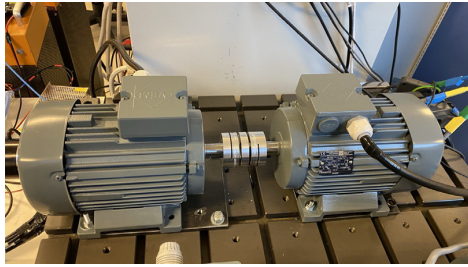


FIGURE 3. Photo of the test rig.

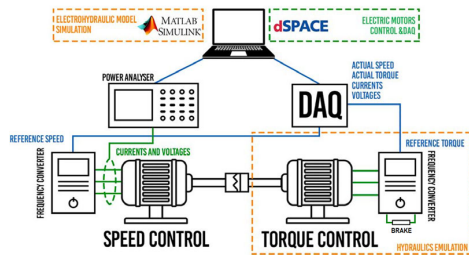


FIGURE 4. Diagram of the test rig.

**A. TEST RIG**

As mentioned earlier, the source of rotational energy in the studied DDH system is the PMSM in Figure 1. The displacement of the pumps is calculated so that the flow created by the pumps is proportional to the chambers of the asymmetric cylinder. The system is closed and contains a minimum number of elements that have direct connections with other parts of the system. Any dynamic changes in the system will somehow affect the operation of the hydraulic pumps, which in turn create a load moment for the PMSM. Theoretically, the entire hydro-mechanical part of the system (i.e., hydraulics and gearbox) can be replaced by a source of load moment. For this purpose, an identical PMSM, which matched the prime mover, was used as the load source. The dynamics of the load EM is determined by the operation of the DDH model developed in MATLAB/Simulink and described in the previous section. A photograph of the actual test rig is shown in Figure 3.

The entire experimental setup includes two PMSMs and two ABB frequency converters that control the motors in different modes. One converter controls the motor in the speed control mode, and the second one operates in the torque control mode, thereby acting as a load. Additionally, a braking resistor is connected to the converter that controls the motor in the torque mode for energy dissipation. Speed and torque control signals are transmitted to the converters via the dSpace MicroLabBox data acquisition system. A HIOKI PW6001 power analyzer was used to measure currents and voltages. Data processing was performed on a personal computer. The schematic diagram of the setup is shown in Figure 4. The main parameters of the electric motors, as specified in the technical data sheet [23], are presented in Table 1.

In this study, the prime mover EM is replaceable and has three options: a healthy PMSM, a PMSM with a

TABLE 1. Electric motor parameters.

VEM motors	IE5-PS2R 90 L4 HW
Nominal current	5 A
Nominal power	2.2 kW
Nominal voltage	280 V
Nominal torque	7 Nm
Maximum torque	28 Nm
Nominal speed	3000 rpm
Nominal frequency	100 Hz
Stator winding resistance	0.8 Ohm
Stator winding inductance	4.5 mH
Power factor	0.99
Efficiency	92%
Moment of inertia	0.0026 kgm <sup>2</sup>

demagnetization fault, and a PMSM with an inter-turn short circuit (ITSC). More detailed information about the faults is provided in the following section.

**B. ELECTRIC MOTOR FAULTS**

Faults in PMSMs can significantly affect their performance, which is particularly critical in NRMMs. Among others, rotor magnet demagnetization and ITSC are the most common and severe fault types [24]. Demagnetization of a PMSM is a serious failure, and in the context of NRMM, it may even pose a safety risk. This fault may lead to reduced torque, efficiency, synchronization problems, increased noise, and even complete motor stalling [25]. Common causes of rotor magnet demagnetization include thermal stress, mechanical wear, and manufacturing inconsistencies [26]. In this paper, the rotor magnet demagnetization was introduced by applying localized thermal stress: specific areas of the rotor were heated for a specified time, while the adjacent areas were actively cooled to prevent unintended demagnetization. As a result, the magnetic field strength in two regions of the rotor north pole decreased by 30.4% and 26.5%, respectively.

An ITSC is also considered to be one of the most critical faults in PMSMs [27]. It can cause to localized overheating. A potential failure mode involves an electrical breakdown between windings and the housing, which can pose a safety hazard for both equipment and personnel. As with demagnetization, this fault can lead to a violation of the rotor-stator synchronization due to the asymmetry of currents in the phases [28]. The ITSC was introduced in Phase U as shown in Figure 5, and the ITSC level of 6% is defined by the reduction of resistance in this phase [29].

**IV. EXPERIMENT DESCRIPTION**

For a correct emulation of the operation of the hydraulic part of the system, both under healthy and faulty conditions, using a PMSM, it is necessary to select an appropriate duty cycle. The duty cycle must reflect the actual operating conditions and the dynamic capabilities of the equipment, given that the behavior of the hydraulic system is usually accompanied by characteristic torque pulsations, which are amplified by in the presence of defects. Accordingly, this section presents calculations of the parameters that confirms

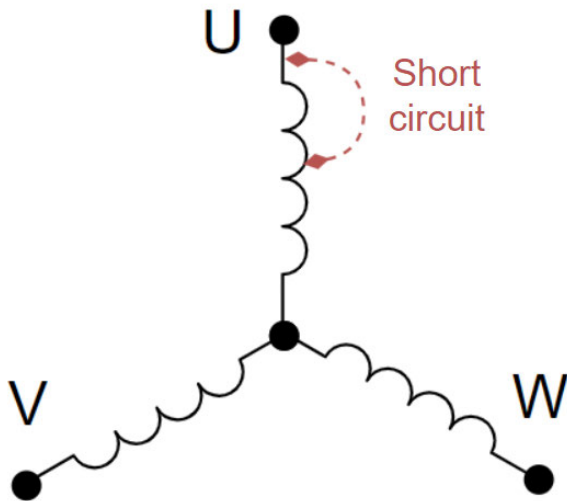


FIGURE 5. ITSC fault implementation.

the suitability of the selected cycle with respect to the capabilities of the studied system.

#### A. WORK CYCLE SELECTION

As described in Section II— modeling, the operation of a DDH system with a pump defect—i.e., a broken gear tooth requires accounting for torque pulsations and accurately determining an appropriate duty cycle. In experiments and simulations, a speed profile as shown in Figure 6 was used, starting at 0 rpm, increased to 500 rpm, then decreased back to 0 rpm, where it was held for 4 seconds before the cycle repeated in the opposite direction. This sequence was repeated five times. In the actual system, the prime mover was connected to the pumps via a T-gearbox. Originally, the gear ratio for this experiment was 1.5:1, but it was modified to 2:1 in the simulation model. This change results in a maximum pump speed of 250 rpm. The changed ratio was also taken into account in the recalculation of the load torque.

Using the maximum pump rotation speed, the frequency of pulsations caused by the pump failure was determined to be approximately 4.167 Hz at the maximum rotation speed of 500 rpm. To evaluate the ability of the motor to reproduce or capture torque pulsations at this frequency, electrical and mechanical time constants were calculated as follows.

The electrical time constant is given as

$$t_e = \frac{L_s}{R_s}, \quad (23)$$

where  $L_s$  is the stator inductance and  $R_s$  is the stator resistance.

The mechanical time constant is calculated as follows:

$$t_m = \frac{J}{B}, \quad (24)$$

where  $J$  is the rotor inertia and  $B$  is the damping coefficient.

The obtained values of  $t_e$  and  $t_m$  are smaller than the pulsation period corresponding to 4.167 Hz ( $T \approx 0.24$ s). This indicates that both the electromagnetic and mechanical

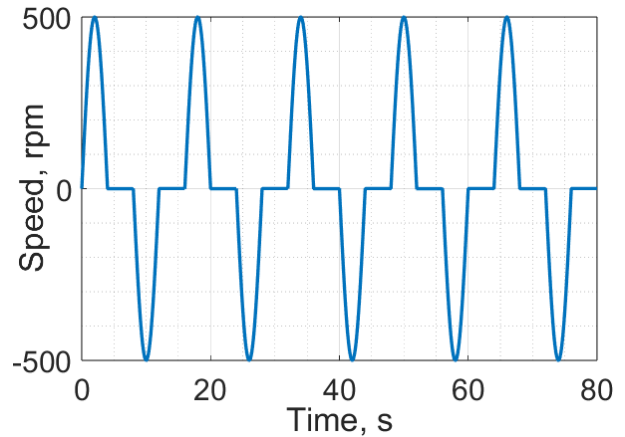


FIGURE 6. Speed profile of the EM.

subsystems of the PMSM can dynamically respond to and reproduce torque pulsations at this frequency without noticeable attenuation. Therefore, the system possesses sufficient bandwidth to accurately emulate the 4.167 Hz oscillations introduced by the pump fault.

The impact of check-valve faults was also studied and found to have an impact on the system dynamics. In particular, the simulation showed that in the DDH system, a dead-zone fault increases the amplitude of the torque jump when the pump reverses, which affects the transient processes of the EM. A leakage fault leads to a loss of pressure when the load rises, increasing the torque required to maintain the system.

In the case of internal cylinder leaks, the effect of the EM depends on the operating modes. If the leak occurs when the load is lowered, the EM load decreases due to the reduced pressure. However, during actively lifting, the leak increases the required torque, as energy is lost. These effects develop gradually, without fluctuations. Taking into account the behavior of the faults, the calculated EM parameters and the adjusted maximum rotation speed, it can be concluded that the selected operating mode allows for an accurate emulation of the dynamic behavior of the system.

Although the payload in the experimental setup remained constant, the total load on the electric motor varied slightly due to transient torque. The theoretical applicability of the method to more strongly varying loads is discussed in Section V.

#### B. EXPERIMENTAL RESULTS

This experiment includes a series of tests of an emulated DDH system under various fault conditions. The tests were conducted on a healthy PMSM, then replaced with a demagnetized motor, then replaced with a demagnetized one, and finally with a PMSM exhibiting ITSC faults. Each PMSM was tested in working cycles with a load simulating a fully functional hydraulic system, along with a check-valve deadband and leakage, and with pump and cylinder faults. All of the machine health combinations are summarized in Table 2.

**TABLE 2. Numeration of fault scenarios.**

Fault scenarios title	EM scenario	Scenario
Healthy EM and healthy hydraulics	21	1
Healthy EM and check valve dead-band fault	21	2
Healthy EM and check valve leakage fault	21	3
Healthy EM and cylinder fault	21	4
Healthy EM and pump fault	21	5
Demagnetized EM and healthy hydraulics	22	6
Demagnetized EM and check valve dead band fault	22	7
Demagnetized EM and check valve leakage fault	22	8
Demagnetized EM and cylinder fault	22	9
Demagnetized EM and pump fault	22	10
Short-circuited EM and healthy hydraulics	23	11
Short-circuited EM and check valve dead-band fault	23	12
Short-circuited EM and check valve leakage fault	23	13
Short-circuited EM and cylinder fault	23	14
Short-circuited EM and pump fault	23	15

As a result, 15 unique scenarios were selected, each of which underwent the previously described work cycle. The cycle was repeated three times to improve data robustness and reduce statistical variance.

During each session, the following data were collected and saved for later use: currents and voltages of the EM operating as a prime mover, shaft speed, and shaft torque. The currents and voltages were measured using a power analyzer, as their accuracy is of particular importance. The speed and torque were recorded by the dSpace system at the output of the frequency converter.

**V. CONDITION MONITORING**

This section presents a fault identification method that analyzes current and voltage signals from the prime mover. These signals are used to detect faults in hydraulic and electrical components. In order to ensure accurate fault detection, a multi-stage data preprocessing technique was utilized, followed by AI-based fault classification.

**A. DATA PREPROCESSING AND FEATURE EXTRACTION**

Raw time-domain data from the PMSM, such as phase currents and voltage, cannot be directly used for classification due to the non-stationary nature of the signals since EM operating cycles introduce periodic changes in electrical signals due to changes in rotation speed and load torque. Even signal segments that appear in a steady-state are unsuitable for fault detection without further transformation. Examples of “raw” signals for various faults are shown in Figure 7. To solve this problem, a multi-stage data processing is used, including domain transformation, filtering and normalization. The complete data transformation pipeline is illustrated in Figure 8.

The preprocessing begins by calculating the reference angular frequency  $\omega_{base}$  as follows:

$$\omega_{base} = \frac{\sum_{n=1}^{\infty} |\omega_n|}{n} \tag{25}$$

Then, at each time step, the angular velocity EM is calculated, after which the data are interpolated onto a uniform coordinate grid, which allows us to obtain a representation of the signal in the domain associated with the angular velocity of the rotor.

Phase currents vary in amplitude and frequency, requiring normalization. For this purpose, the load torque profile obtained from the prime mover is utilized. In this process, the base torque  $T_{base}$  is determined for the observation period as a certain value, after which the normalization coefficient  $k_{norm}$  is calculated, which is then used to scale the signals.

$$k_{norm}(t) = \frac{T_{base}(t)}{T_{em}(t)}, \tag{26}$$

$$i_{norm}(t) = i(t) k_{norm}(t). \tag{27}$$

After domain transformation and amplitude normalization, the signal is filtered using the exponential moving average (EMA) algorithm. This preprocessing concept also provides theoretical applicability under varying-load conditions, as it compensates for load-dependent amplitude and frequency variations. However, additional training data may be required for accurate classification under strongly dynamic loads. EMA was selected for its merit of sensitivity to rapid changes and noise reduction. This ensures sensitivity to abrupt changes in data, while maintaining the required level of filtering. The final stage of data preprocessing involves normalization, ensuring that the data is located in a given range suitable for feature extraction.

Feature extraction is necessary as using raw data would result in very low accuracy due to the high variability of signal characteristics. For this process, the time series data was segmented into intervals of 1000 points, after which the key statistical features were calculated for each segment: mean, median, minimum, maximum, root mean square (RMS), kurtosis, skewness, shape factor, impulse factor, peak factor, and gap factor. Additionally, the following features were included: variance, mean absolute deviation (MAD), entropy, peak-to-peak amplitude, and zero-crossing frequency. As a result, 16 features were utilized.

$$\text{Var}(X) = \frac{1}{N} \sum_{i=1}^N (x_i - \mu)^2, \tag{28}$$

$$\text{MAD}(X) = \frac{1}{N} \sum_{i=1}^N |x_i - \mu|, \tag{29}$$

$$H(X) = - \sum_{i=1}^N p(x_i) \log_2 p(x_i), \tag{30}$$

$$\text{ZCR}(X) = \frac{1}{N-1} \sum_{i=1}^{N-1} \mathbf{1}(x_i \cdot x_{i+1} \leq 0), \tag{31}$$

$$\text{P2P}(X) = \max(x) - \min(x), \tag{32}$$

where,  $x_i$  are the sample values,  $\mu$  is the mean,  $p(x_i)$  is a the probability of occurrence of the value  $x_i$  in the sample, and  $\mathbf{1}$  is an indicator function that equals 1 if the product of

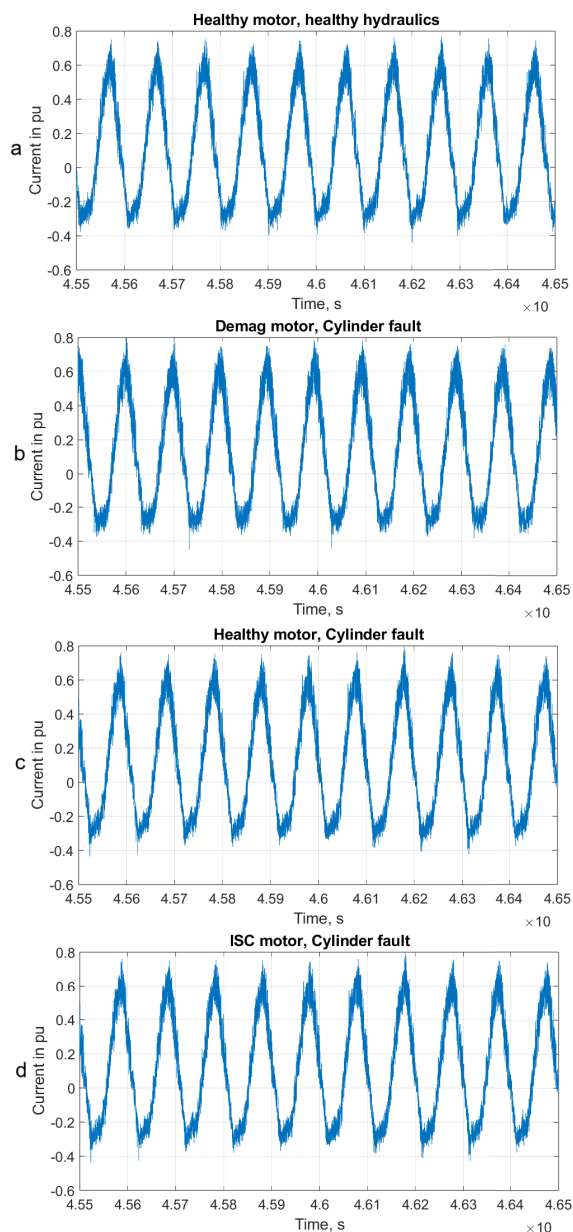


FIGURE 7. Unprocessed currents comparison.

the neighboring values is less or equal to zero (i.e., a zero-crossing has occurred) and 0 if otherwise.

To exclude uninformative features, the minimum redundancy maximum relevance (MRMR) algorithm was applied to automatically exclude all voltage-related parameters. Then the remaining 48 features were subjected to variance analysis (ANOVA) as in the previous study [17]. As a result, 38 features were selected in the classifier training.

**B. CLASSIFICATION**

The selection of SVM was also based on its ability to efficiently process data and separate it into well-defined classes [30]. In addition, findings from our previous work [17] showed that the cubic SVM achieved an accuracy comparable to that of the neural network model while

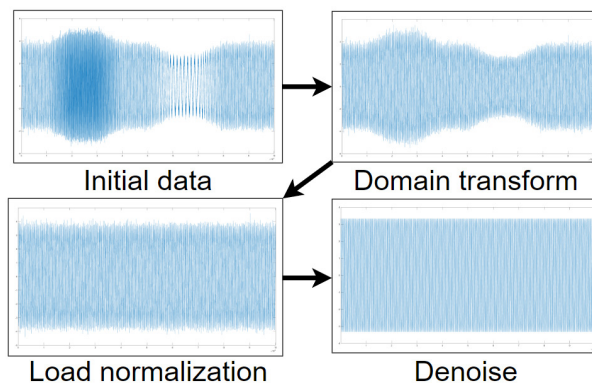


FIGURE 8. Preprocessing of data.

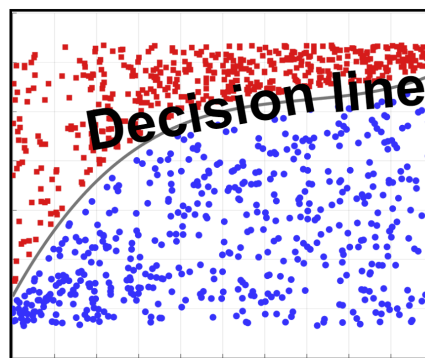


FIGURE 9. Cubic SVM algorithm representation.

requiring significantly less computation time for classification. Considering these earlier results and the relatively small dataset used in the present research, SVM was selected as a balanced approach that combines accuracy, efficiency, and interpretability. In principle, the cubic SVM applies a third-degree polynomial kernel to separate data into distinct classes. The operating principle of the method is illustrated in Figure 9.

In scenarios where the performance of cubic SVM is insufficient, fine Gaussian SVM is used. This method determines separating hyperplanes in high-dimensional spaces [31], taking into account both pronounced and subtle nonlinear dependencies between features. If separation in the current feature space is insufficient, the algorithm projects the data into higher dimensions [32]. It can theoretically simplify the search for the optimal separating hyperplane. An example of fine Gaussian SVM performance is shown in Figure 10.

The classification model was trained using preprocessed data (currents) obtained from two experimental runs. The first portion of the data was utilized to train the model, and the second was used for validation. This approach is more rigorous than single-sample cross-validation. To evaluate the accuracy of the model, an independent dataset obtained during a separate experiment was utilized. This allowed us to evaluate the generalization capability of the model and its performance under conditions close to real ones.

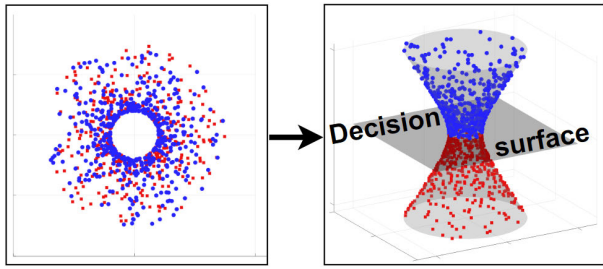


FIGURE 10. Fine Gaussian SVM algorithm representation.

VI. RESULTS AND DISCUSSION

Before classifying all of the selected 16 scenarios, the data were grouped according to the EM condition. This initial grouping was conducted in order to separate the scenarios into broader fault categories to evaluate how effectively the classification model can detect different EM fault types. As a result, only three faulty cases were formed. In Table 2 a healthy motor (Class 21), a motor with partial demagnetization (Class 22), and a motor with ITSC (Class 23) are shown. The classification was performed using the cubic SVM method. The confusion matrix shown in Figure 11 illustrates the classification results.

As seen from Figure 11, the classification of electrical faults showed high overall classification accuracy across all three scenarios and represents the true positive rate (TPR) and false negative rate (FNR) for each class. Class 21 (healthy motor) achieved a TPR of 92.1%, with misclassifications of 7.5% as Class 22 (demagnetized EM) and 0.4% for Class 23 (ITSC EM). For Class 22, the TPR was 92.2%, while 7.2% were misclassified as healthy motors and 0.6% as short-circuited motors. In the case of the motor with Class 23, the TPR reached 94.2%, while 4.5% were misclassified as demagnetized motors and 1.3% as healthy motors. It can be seen that the misclassification rates between healthy and demagnetized motors are quite close. This has a significantly smaller effect on the performance of PMSM compared to the same ITSC.

The highest classification accuracy was achieved for the ITSC motor (Class 23), where the FNR was 5.8%, while Classes 21 and 22 showed slightly higher FNR values of 7.9% and 7.8%, respectively.

The obtained results indicate that the classifier performs best in classifying motors with ITSC, which may suggest that this type of faults has the most prominent features. At the same time, demagnetized and serviceable motors are sometimes mistakenly classified as each other, reflecting the similarity of their characteristics. Nevertheless, the overall classification accuracy remains high, confirming the reliability of the utilized data processing algorithm.

Moving to the full classification analysis, all 16 fault cases as shown in Table 2 were used. As in the previous experiment, the Cubic SVM method was utilized for classification, but the results showed significantly lower accuracy compared to

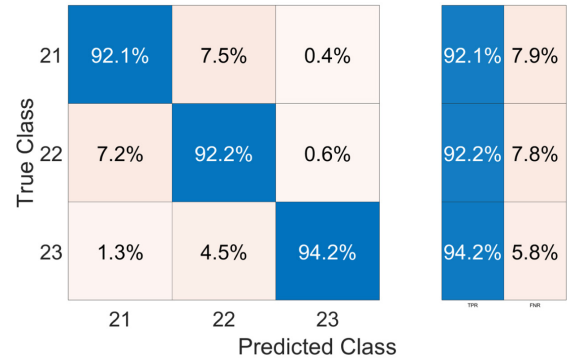


FIGURE 11. Classification of EM-related cases.

the EM classification. This is demonstrated by the confusion matrix in Figure 12.

As observed in the confusion matrix, there is significant overlap between the classes, especially within the EM case binding. This makes fault discrimination ineffective. In particular, this was reflected in some classes, showing low TPR values and high FNR values. The maximum recorded TPR was 27.6%, while in the previous experiment, the TPR for individual classes reached 94.2%. The drop in overall classification accuracy indicates that increasing class complexity introduces greater feature overlap, particularly between EM and hydraulic fault types. This is probably attributed to higher intra-class variance and overlapping characteristics among the faults. The most significant confusion occurred within EM scenarios (among Classes 1–5, 6–10, and 11–15). This indicates that while the classifier still distinguishes EM faults well, it struggles to cope with hydraulic faults. This confusion can be attributed to the limited sensitivity of the extracted statistical features to subtle hydraulic variations and to the nonlinear coupling between the electrical load and the hydraulic resistance, which causes overlapping feature distributions and reduces class separability. The results at this stage indicate that adjustments are required in the data processing to improve the fault classification.

To improve the accuracy of fault detection, the SVM kernel was upgraded to the fine Gaussian. After replacing the kernel, the model was trained using the standard settings and the classification results are shown in Figure 13.

Overall, the core replacement resulted in more uniform results across the confusion matrix. After switching to the fine Gaussian SVM with default parameters, the overall classification accuracy improved due to the higher flexibility of the Gaussian kernel in capturing nonlinear dependencies. However, the issues observed in the previous configuration persisted and, in some cases, became more pronounced. This effect can be explained by the increased sensitivity of the model to dominant feature patterns, which enhances the recognition of well-separated classes but simultaneously amplifies misclassifications between classes with overlapping feature distributions. It is noticeable that the percentage

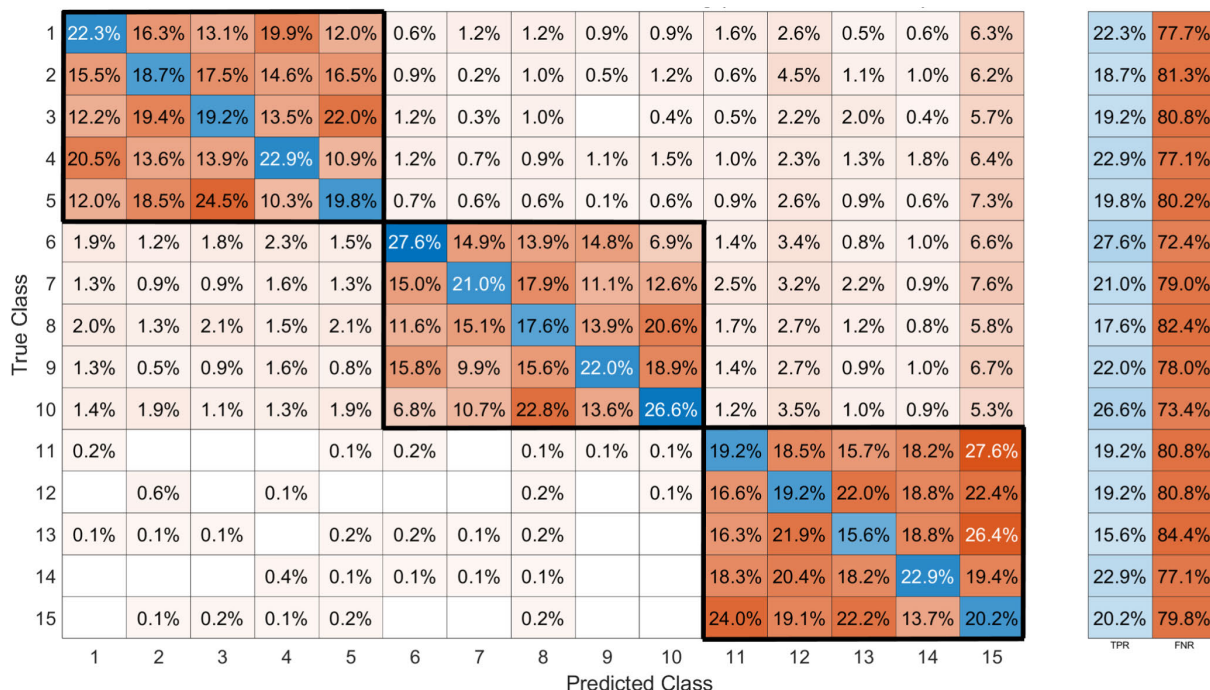


FIGURE 12. Classification of 15 classes (cubic SVM, low accuracy).

of correct identifications has significantly increased, although in some fault cases, an increase in false positives was observed. For example, Class 5 is now identified with 88.1% TPR, and Class 15 with 71.6%, which is significantly higher than in the previous experiment. At the same time, almost all classes retained confusion with certain other classes, even significantly increasing the percentage of false positives. However, this phenomenon is observed only within the EM groups. For example, the misidentification of Class 4 as Class 1 increased from 20.5% to 46.6%, while its confusion with other classes decreased significantly. Classes in the range of 6–10 remain difficult to classify and the highest error rate is observed in this range (the minimum TPR value is 25.8%). The obtained results, although suggesting a reduction in disparity between TPR and FNR values, also indicate difficulties in accurately distinguishing faults related to the hydraulic system. To overcome these difficulties, it was decided to use the same kernel, but to fine-tune the model more accurately.

In particular, to improve the classifier performance, the kernel scaling mode was changed to automatic under Matlab control and the multiclass classification method was replaced from One-vs-One to One-vs-All. This allowed achieving a significant increase in classification accuracy compared to the previous examination. The updated results are shown in Figure 14.

As observed from the confusion matrix, the TPR values for most classes now exceed 80%. In particular, classes 1, 2, 4–7, 9, and 15 are identified with a TPR of 91.3% or higher. The degree of cross-classification between classes has

been significantly reduced. The average FNR and TPR values are 14.7% and 85.3%, respectively. Despite the significant improvements, certain classes still exhibit relatively high FNR values. Class 11 (TPR = 60.9%, FNR = 39.1%) and Class 14 (TPR = 61.6%, FNR = 38.4%) continue to show high classification error rates. This indicates that the model still has difficulty distinguishing between certain types of hydraulic faults that have similar effects on the electrical parameters of the system. This can be explained by the fact that some hydraulic component failures, such as leaks or valve malfunctions, lead to similar changes in EM performance, making them difficult to differentiate.

In addition, Classes 12, 13, and 14 also show comparatively low accuracy levels. Thus, it can be assumed that short-circuited EMs significantly complicate the identification of hydraulic faults due to their “masking” effect. The masking effect arises from electrical and mechanical distortions produced by the ITSC, which introduces negative-sequence currents, torque ripple, and low-order harmonics overlapping with the frequency bands where hydraulic fault signatures are present. These components dominate the current and pressure spectra, reducing the distinguishability of hydraulic features and their sensitivity to fault-induced variations. Additionally, the closed-loop control of the PMSM tends to compensate for these asymmetries, generating further signal modulations that obscure hydraulic effects. However, for a more detailed explanation and quantitative validation of this interaction, further investigation and analysis are required. The results from all three models are summarized in Table 3.



**TABLE 3.** TPR and FNR comparison of models across 15 scenarios.

Scenario	Cubic SVM		FG SVM		FG SVM Tuned	
	TPR	FNR	TPR	FNR	TPR	FNR
1	22.3	77.7	44.6	55.4	<b>93.4</b>	<b>6.6</b>
2	18.7	81.3	43.4	56.6	<b>96.1</b>	<b>3.9</b>
3	19.2	80.8	43.8	56.2	<b>84.7</b>	<b>15.3</b>
4	22.9	77.1	37.6	62.4	<b>93.0</b>	<b>7.0</b>
5	19.8	80.2	88.1	11.9	<b>94.0</b>	<b>6.0</b>
6	27.6	72.4	37.4	62.6	<b>94.4</b>	<b>5.6</b>
7	21.0	79.0	53.3	46.7	<b>96.1</b>	<b>3.9</b>
8	17.6	82.4	30.5	69.5	<b>84.1</b>	<b>15.9</b>
9	22.0	78.0	25.8	74.2	<b>91.3</b>	<b>8.7</b>
10	26.6	73.4	46.7	53.3	<b>88.2</b>	<b>11.8</b>
11	19.2	80.8	43.9	56.1	<b>60.9</b>	<b>39.1</b>
12	19.2	80.8	36.9	63.1	<b>78.0</b>	<b>22.0</b>
13	15.6	84.4	40.1	59.9	<b>71.9</b>	<b>28.1</b>
14	22.9	77.1	42.1	57.9	<b>61.6</b>	<b>38.4</b>
15	20.2	79.8	71.6	28.4	<b>91.9</b>	<b>8.1</b>

consistently when the electric motor operates in a healthy or partially demagnetized state, while the presence of ITSC faults introduces additional uncertainty due to their masking effect. This decrease in accuracy under mixed fault conditions highlights the mutual influence of electrical and hydraulic faults, which addresses question (2).

The optimized model significantly enhances fault classification performance, particularly in complex multiclass scenarios. However, further refinement and expansion of the feature space are needed to more accurately distinguish similar hydraulic faults. The obtained results confirm the effectiveness of the utilized approach and provide a foundation for further improvements in diagnostic methods for electro-hydraulic systems.

## VII. CONCLUSION

The results of the study demonstrate the high efficiency of the proposed AI-based method for diagnosing faults in electro-hydraulic systems. The machine learning analysis of electrical signals enabled accurate detection of both individual and combined faults, as confirmed by experimental evaluation. The TPR of up to 94.2% was achieved in classifying EM states, while the fine Gaussian SVM with parameter optimization provided average TPR levels above 85% and up to 91.3% across all scenarios. Overall, eight fault scenarios were identified with an overall classification accuracy higher than 90%; three scenarios achieved a TPR between 80% and 90%; and four scenarios showed a TPR between 60% and 80%. These findings confirm the achievable diagnostic precision of the proposed method and answer question (1), concerning the attainable an overall classification accuracy of fault detection using only electrical measurements.

The lower overall classification accuracy observed in the four least precise scenarios reveals a new and significant finding: ITSC produces a masking effect that reduces the distinguishability of hydraulic faults. This observation highlights the mutual influence of electrical and hydraulic faults within the system, providing an experimental explanation

for question (2). It also introduces a new understanding of how overlapping fault signatures can interfere in AI-based diagnostic models, emphasizing the need for enhanced feature extraction and data preprocessing techniques.

In conclusion, this study demonstrates that analyzing electric motor signals using artificial intelligence methods enables the identification of both electrical and hydraulic faults in DDH systems. The obtained results contribute to the development of approaches for sensorless diagnostics and intelligent predictive maintenance of electro-hydraulic machines. The achieved diagnostic accuracy—exceeding 90% in most fault scenarios—confirms the potential of the proposed method for further research and practical implementation. These findings pave the way for the creation of advanced condition-monitoring systems for the next generation of intelligent mobile machinery, offering improved reliability and efficiency of electro-hydraulic equipment while simultaneously reducing operational and maintenance costs.

Future research will focus on addressing the identified limitations in three main directions. First, the range of fault types and their combinations will be expanded to more comprehensively capture the interactions between electrical and hydraulic defects. Second, time–frequency domain features (e.g., wavelet- or spectrogram-based) will be investigated to enhance fault separability. Third, transfer learning techniques will be employed to improve the generalizability of the model under varying operating conditions and combined fault scenarios. These steps are expected to enhance the robustness and adaptability of the proposed diagnostic approach.

## REFERENCES

- [1] R. Hagan, E. Markey, J. Clancy, M. Keating, A. Donnelly, D. J. O'Connor, L. Morrison, and E. J. McGillicuddy, "Non-road mobile machinery emissions and regulations: A review," *Air*, vol. 1, no. 1, pp. 14–36, Nov. 2022.
- [2] (2016). *Regulation (EU) 2016/1628 of the European Parliament and of the Council of 14 September 2016 on Requirements Relating to Gaseous and Particulate Pollutant Emission Limits and Type-Approval for Internal Combustion Engines for Non-Road Mobile Machinery*. Accessed: Mar. 6, 2025. [Online]. Available: <https://eur-lex.europa.eu/eli/reg/2016/1628/oj/eng>
- [3] (1997). *Directive 97/68/EC of the European Parliament and of the Council of 16 December 1997 on the Approximation of the Laws of the Member States Relating to Measures Against the Emission of Gaseous and Particulate Pollutants From Internal Combustion Engines to Be Installed in Non-Road Mobile Machinery*. Accessed: Mar. 6, 2025. [Online]. Available: <https://eur-lex.europa.eu/eli/dir/1997/68/oj>
- [4] Ministry of Economic Affairs and Employment of Finland. (2022). *Publications of the Ministry of Economic Affairs and Employment 2022:55*. Accessed: Mar. 6, 2025. [Online]. Available: <https://julkaisu.t.valtionneuvosto.fi/handle/10024/164323>
- [5] J. Park, H. Lim, S. Kim, J. Song, and Y. K. Lee, "Modeling and validation of driving performance of electric vehicle converted from internal combustion engine vehicle," *IEEE Trans. Transport. Electric.*, vol. 11, no. 1, pp. 486–498, Feb. 2025.
- [6] M. Ferrari, C. Dai, B. Daniele, and U. Stefano, "Electrification of non-road mobile machinery: A tool for motor selection," in *Proc. Int. Conf. Electr. Mach. (ICEM)*, Sep. 2024, pp. 1–7.
- [7] G. Goswami, A. Tupitsina, S. Jaiswal, C. Nutakor, T. Lindh, and J. Sopenan, "Comparison of various hybrid electric powertrains for non-road mobile machinery using real-time multibody simulation," *IEEE Access*, vol. 10, pp. 107631–107648, 2022.

- [8] T. Koiito, O. Caloni, H. Kauranne, T. Minav, and M. Pietola, "Enhanced energy efficiency of industrial application by direct driven hydraulic unit," in *Proc. Global Fluid Power Soc. PhD Symp. (GFPS)*, Jul. 2018, pp. 1–6.
- [9] E. N. B. Aidoo, "A comparative analysis of electro-hydrostatic actuators and a conventional valve-controlled actuator for heavy-duty mobile applications," Master's thesis, Fac. Eng. Natural Sci., Tampere Univ., Tampere, Finland, Nov. 2020.
- [10] S. Zhang, T. Minav, and M. Pietola, "Decentralized hydraulics for micro excavator," in *Proc. 15th Scand. Int. Conf. Fluid Power (SICFP)*, Dec. 2017, pp. 187–195. [Online]. Available: <http://www.ep.liu.se/ecp/contents.asp?issue=144>
- [11] T. Minav, C. Bonato, P. Sainio, and M. Pietola, "Direct driven hydraulic drive," in *Proc. The 9th Int. Fluid Power Conf.*, Aachen, Germany, Mar. 2014.
- [12] Y. Shang, X. Li, H. Qian, S. Wu, Q. Pan, L. Huang, and Z. Jiao, "A novel electro hydrostatic actuator system with energy recovery module for more electric aircraft," *IEEE Trans. Ind. Electron.*, vol. 67, no. 4, pp. 2991–2999, Apr. 2020.
- [13] M. Kumar, "A survey on electro hydrostatic actuator: Architecture and way ahead," *Mater. Today, Proc.*, vol. 45, pp. 6057–6063, Jan. 2021.
- [14] M. Ghanbari, W. Kinsner, and N. Sepehri, "Detection of faults in electro-hydrostatic actuators using feature extraction methods and an artificial neural network," in *Proc. IEEE World AI IoT Congr. (AIoT)*, Jun. 2022, pp. 01–07.
- [15] J. Miao, J. Wang, D. Wang, and Q. Miao, "Experimental investigation on electro-hydraulic actuator fault diagnosis with multi-channel residuals," *Measurement*, vol. 180, Aug. 2021, Art. no. 109544.
- [16] A. Abdul Azeez, X. Han, V. Zakharov, and T. Minav, "AI-based condition monitoring of hydraulic valves in zonal hydraulics using simulated electric motor signals," in *Proc. ASME/BATH Symp. Fluid Power Motion Control*, Oct. 2021, p. 001.
- [17] V. Zakharov, A. Abdul Azeez, X. Han, and T. Minav, "The impact of electric drive structures on sensorless AI-based hydraulic valve fault classification," in *Proc. ASME/BATH Symp. Fluid Power Motion Control*, Oct. 2023, p. 001.
- [18] C. Yildirim, A. M. Franco-Pereira, and R. E. Lillo, "Condition monitoring and multi-fault classification of hydraulic systems using multivariate functional data analysis," *Heliyon*, vol. 11, no. 1, Jan. 2025, Art. no. e41251. [Online]. Available: <https://ssrn.com/abstract=4982474>
- [19] G. Wrat, P. Ranjan, and J. C. Das, "Leakage and its effects in various hydraulics driven system," *Int. J. Control Theory Appl.*, pp. 4355–4359, 2016.
- [20] X. Zhao, S. Zhang, C. Zhou, Z. Hu, R. Li, and J. Jiang, "Experimental study of hydraulic cylinder leakage and fault feature extraction based on wavelet packet analysis," *Comput. Fluids*, vol. 106, pp. 33–40, Jan. 2015.
- [21] W. Yin, J. Zhang, X. Wang, Q. Zhang, and Y. Li, "Volumetric efficiency degradation prediction of axial piston pump based on friction and wear test," *Heliyon*, vol. 10, no. 17, Sep. 2024, Art. no. e37334, doi: 10.1016/j.heliyon.2024.e37334.
- [22] F. Sedri and A. Riasi, "Investigation of leakage within an external gear pump with new decompression slots: Numerical and experimental study," *J. Brazilian Soc. Mech. Sci. Eng.*, vol. 41, no. 5, pp. 1–12, May 2019, doi: 10.1007/s40430-019-1717-8.
- [23] (Sep. 2022). *Permanent-Magnet Synchronous Energy Saving Motors—Data Sheet*. [Online]. Available: <https://www.vem-group.com>
- [24] A. Demirel, O. Keysan, M. El-Dalahmeh, and M. Al-Greer, "Non-invasive real-time diagnosis of PMSM faults implemented in motor control software for mission critical applications," *Measurement*, vol. 232, Jun. 2024, Art. no. 114684.
- [25] F. Huang, X. Zhang, G. Qin, J. Xie, J. Peng, S. Huang, Z. Long, and Y. Tang, "Demagnetization fault diagnosis of permanent magnet synchronous motors using magnetic leakage signals," *IEEE Trans. Ind. Informat.*, vol. 19, no. 4, pp. 6105–6116, Apr. 2023.
- [26] M. Baranski, W. Szelag, and W. Lyskawinski, "Analysis of the partial demagnetization process of magnets in a line start permanent magnet synchronous motor," *Energies*, vol. 13, no. 21, p. 5562, Oct. 2020, doi: 10.3390/en13215562.
- [27] J. Yuan, X. Dong, G. Niu, and X. Ge, "Fault detection of synchronous motor inter-turn short circuit based on current residual harmonic characteristics," *Proc. Inst. Mech. Eng., C, J. Mech. Eng. Sci.*, vol. 239, no. 15, pp. 6238–6257, Apr. 2025.
- [28] M. Zafarani, E. Bostanci, Y. Qi, T. Goktas, and B. Akin, "Interturn short-circuit faults in permanent magnet synchronous machines: An extended review and comprehensive analysis," *IEEE J. Emerg. Sel. Topics Power Electron.*, vol. 6, no. 4, pp. 2173–2191, Dec. 2018.
- [29] M. S. Mahmoud, V. K. Huynh, J. S. L. Senanyaka, and K. G. Robbersmyr, "Robust multiple-fault diagnosis of PMSM drives under variant operations and noisy conditions," *IEEE Open J. Ind. Electron. Soc.*, vol. 4, pp. 762–772, 2023, doi: 10.1109/OJIES.2024.3350443.
- [30] A. Ben Slama, Y. Amri, A. Fnaiech, and H. Sahli, "Automated ECG arrhythmia classification using hybrid CNN-SVM architectures," *J. Nonlinear Electrochem. Syst.*, 2025, doi: 10.1016/j.jnlest.2025.100316.
- [31] A. Y. Shdefat, N. Mostafa, Z. Al-Arnaout, Y. Kotb, and S. Alabed, "Optimizing HAR systems: Comparative analysis of enhanced SVM and k-NN classifiers," *Int. J. Comput. Intell. Syst.*, vol. 17, no. 1, pp. 1–32, Jun. 2024.
- [32] J. Suykens. (2005). *Support Vector Machines and Kernel Based Learning*. [Online]. Available: <http://www.esat.kuleuven.ac.be/sista/lssvmlab/>



**VIACHESLAV ZAKHAROV** received the Master of Science degree in mechatronics from St. Petersburg Electrotechnical University "LETI," with exchange studies with Aalto University and the University of Agder. He is currently a Doctoral Researcher with Tampere University, Finland, specializing in electric drive control and electro-hydraulic systems. His contributions include control system development, electrification, and condition monitoring of electro-hydraulic applications. His professional experience includes roles in research and development, software development, and automation engineering. His published works contribute to improving the efficiency and reliability of electro-hydraulic systems. His research focuses on AI-based fault diagnostics, hybrid powertrains, and power electronics. His research interests include mathematical modeling, experimental testing, and AI-driven diagnostics.



**VAN KHANG HUYNH** received the D.Sc. (Tech.) degree in electrical engineering from Aalto University, Espoo, Finland, in 2012. He was an Associate Professor in electrical power engineering with the University of Agder, Grimstad, Norway, from 2013 to 2019, where he is currently a Full Professor with the Department of Engineering Sciences and leading the Research Group—Intelligent Monitoring. His research interests include electrical machines, applied AI for condition-based maintenance, and applied power electronics. He is serving as an Associate Editor for IEEE Transactions on Transportation Electrification.



**TATIANA MINAV** (Member, IEEE) received the M.Sc. and D.Sc. degrees from Lappeenranta University of Technology (LUT), Finland, in 2008 and 2011, respectively. She has more than 15 years of experience working on improving the efficiency of heavy-duty mobile machines. She is currently an Associate professor with Tampere University, Finland. Her current research interests include zonal hydraulics, failure detection and monitoring systems, thermal hydraulics simulation, and energy recovery systems for heavy-duty mobile machines.

...